Article

Friction Stir Welding of 1Cr11Ni2W2MoV Martensitic Stainless Steel: Numerical Simulation Based on Coupled Eulerian Lagrangian Approach Supported with Experimental Work

Mohamed Ragab [1,2], Hong Liu [1,*], Guan-Jun Yang [1] and Mohamed M. Z. Ahmed [3,4]

1   State Key Laboratory for Mechanical Behavior of Materials, Xi'an Jiaotong University, Xi'an 710049, China; Mohameb.r@stu.xjtu.edu.cn (M.R.); ygj@mail.xjtu.edu.cn (G.-J.Y.)
2   Department of Mechanical Engineering (Production and Design), Shoubra Faculty of Engineering, Benha University, Cairo 11629, Egypt
3   Mechanical Engineering Department, College of Engineering at Al Kharj, Prince Sattam Bin Abdelaziz University, Al Kharj 16273, Saudi Arabia; moh.ahmed@psau.edu.sa
4   Department of Metallurgical and Materials Engineering, Faculty of Petroleum and Mining Engineering, Suez University, Suez 43512, Egypt
*   Correspondence: hongliu@xjtu.edu.cn

Abstract: 1Cr11Ni2W2MoV is a new martensitic heat-resistant stainless steel utilized in the manufacturing of aero-engine high-temperature bearing components. Welding of this type of steel using fusion welding techniques causes many defects. Friction stir welding (FSW) is a valuable alternative. However, few investigations have been performed on the FSW of steels because of the high melting point and the costly tools. Numerical simulation in this regard is a cost-effective solution for the FSW of this steel in order to optimize the parameters and to reduce the number of experiments for obtaining high-quality joints. In this study, a 3D thermo-mechanical finite element model based on the Coupled Eulerian Lagrangian (CEL) approach was developed to study the FSW of 1Cr11Ni2W2MoV steel. Numerical results of metallurgical zones' shape and weld appearance at different tool rotation rates of 250, 350, 450 and 550 rpm are in good agreement with the experimental results. The results revealed that the peak temperature, plastic strain, surface roughness and flash size increased with an increase in the tool rotation rate. Lack-of-fill defect was produced at the highest tool rotation rate of 650 rpm. Moreover, an asymmetrical stir zone was produced at a high tool rotation rate.

Keywords: friction stir welding; 1Cr11Ni2W2MoV steel; numerical simulation; Coupled Eulerian Lagrangian; flash formation

1. Introduction

1Cr11Ni2W2MoV heat-resistant steel is commonly used in aero-engine high-temperature components. Welding is the technique most used to fabricate complex shapes. However, the traditional fusion welding methods cause many solidification defects and bad mechanical properties when used to join this type of steel. Jia and Yue [1] reported that the heat affected zone (HAZ) width of a tungsten inert gas (TIG) welded 1Cr11Ni2W2MoV joint was 14 mm, while the weld width was 4.8 mm. In addition, the HAZ showed a high reduction in the fatigue limit and tensile strength. Yuan et al. [2] studied the microstructure and mechanical properties of flash welded 1Cr11Ni2W2MoV steel. They found that the weld microstructure contains martensite and delta ferrite. Moreover, quenching and tempering heat treatments were required to improve joint plasticity and impact toughness. On the other hand, Zhang et al. [3] used diffusion bonding to join 1Cr11Ni2W2MoV steel. They reported that the surface was required to be finished by 2000# grit SiC paper produce good joint quality. However, the process was very time consuming, and the joint size was limited to the available equipment. Consequently, finding new welding techniques for 1Cr11Ni2W2MoV heat resistant steel is a crucial issue.

Friction stir welding (FSW) is a solid-state welding technique invented in 1991 by The Welding Institute (TWI) for the main purpose of joining aluminum alloys [4]. The heat generated due to the plastic deformation and friction between the tool and workpiece material plasticizes the material below the tool shoulder and around the pin. Thus, the plasticized material is welded as the tool traverses in the solid state under the tool pressure and stirring. The heat input and peak temperature during the process are lower than those produced during the traditional fusion welding methods. Thus, the microstructure changes away from the nugget zone are smaller after the FSW. The welds are manufactured with low distortion, residual stress and solidification defects [5]. Moreover, FSW can reduce the energy consumed compared to fusion welding by up to 60% [6].

The FSW parameters such as tool rotation, welding speed, plunge depth, plunge rate and tool tilt angle should be selected carefully to avoid or reduce the welding defects. It is well known that tool rotation and welding speed play the most significant role in the FSW process. The rotation speed is mainly responsible for generating the heat and stirring the material at the tool–workpiece interface, while the welding speed controls the cooling rate after welding [7]. To create a good joint, a suitable combination of tool rotation and welding speed is crucial.

To date, FSW becomes one of the most powerful techniques in joining low softening temperature alloys such as aluminum and magnesium alloys [8–11]. However, there is a great interest in the last decade in using FSW to join high softening temperature materials such as steel [12,13]. The major challenges in the welding of steels such as carbon steel (CS), high strength steel (HSS) and stainless steel (SS) by FSW are the expensive tool material and choosing suitable welding parameters [14]. Many tool materials are utilized to weld steel by FSW. The polycrystalline boron nitride (PCBN) [15,16] and tungsten-based refractory metals [17–19] are the FSW tool materials most commonly used for steel. Several studies have been performed to join stainless steel by FSW. The FSW of ferritic stainless steel [13,20] and austenitic stainless steel [21,22] have been carried out. However, no investigations have studied the feasibility of using FSW to join 1Cr11Ni2W2MoV martensitic heat-resistant steel due to its high hardness and the severe tool wear that might occur during welding.

Numerical simulation is an advantageous and successful method to study the FSW process. Compared to the experimental work, the visualization of thermal cycles, surface features and material flow after each stage of the FSW can be easily determined with low effort and cost through numerical modeling. Moreover, numerical simulation can be used to choose the proper welding parameters from a wide range with low cost [23]. Accordingly, different modeling methods such as computational fluid dynamics (CFD), Lagrangian, Eulerian, and arbitrary Lagrangian Eulerian (ALE) methods have been used to study the FSW process.

Almoussawi et al. [24] developed a 3D CFD model to simulate FSW of a 6 mm thick DH36 steel plate in a Eulerian domain. They found that the temperature measured by the thermocouple and CFD model was in good agreement at high welding speed. In addition, the strain rate was enhanced with increasing tool rotation, while increasing the welding speed resulted in increasing the shear stress on the tool surface. Moreover, the optimum range of the tool rotation and welding speed was below 550 rpm and between 100 to 350 mm/min, respectively. Golegrove and Shercliff [25] developed a CFD code, FLUENT, to simulate the material flow around two tools with trivex-based geometry. They reported that the traversing and down forces decreased when using the trivex tools compared to the triflute one. Additionally, they used the streamline planes to understand the material flow around the tool pin and found that the triflute tool has a strong augering action. Although the CFD method had been used successfully to simulate the FSW process [26,27], CFD cannot model the material hardening and elastic properties. In addition, the full sticking conditions assumed between the tool and workpiece material lead to simulation errors in tool reactions and joining temperature [23].

Lagrangian and Eulerian approaches are other methods to simulate the FSW process. The material position relative to nodes remains fixed in the Lagrangian method, while

nodes stay fixed and material moves inside the fixed mesh in the Eulerian one. Thus, the Lagrangian method is suitable to simulate the process outside the processed zone, while the Eulerian approach is good in modeling the material flow [28]. With advances in numerical simulation, the arbitrary Lagrangian Eulerian (ALE) method was developed. Guerdoux and Fourment [29] developed an adaptive ALE formulation to simulate the temperature distribution and material flow during the FSW of 6061 aluminum alloy. They used the Forge 3 FE software to develop their model. Non-steady phases of FSW were simulated as well as the steady phase. Fourment et al. [30] utilized the same software used by Guerdoux and Fourment [29] to model the FSW defect. Meyghani et al. [31] used ALE and a smoothed particle hydrodynamics (SPH) formulation to study the FSW of 6061-T6 aluminum alloy. The results showed that the temperature distribution was symmetric, and the peak temperature increased with increasing the tool rotation. However, the weld surface features and equivalent plastic strain were not studied. Simulation of FSW of aluminum and lightweight alloys was successfully done by the ALE method. However, severe plastic deformation in the SZ caused severe mesh distortion and precocious simulation failure with the ALE formulation [32]. Unlike the ALE formulation, the Coupled Eulerian Lagrangian (CEL) method can simulate the FSW process with severe plastic deformation without precocious failure of the simulation. The CEL method aims to capture the advantages of the Lagrangian and Eulerian approaches. Ansari et al. [32] developed a CEL model to simulate the defects formed during friction stir processing (FSP) of AA 5083-H111 aluminum plate. They did not study the effect of the FSP parameters on the thermal cycle and surface appearance or flash formation.

In the present study, a 3D thermo-mechanical finite element model based on the Coupled Eulerian Lagrangian (CEL) method was developed, using Abaqus/Explicit, to simulate the FSW of 1Cr11Ni2W2MoV heat-resistant martensitic stainless steel. In this model, the thermal cycles at the stir zone (SZ) and the heat affected zone (HAZ) were investigated carefully. In addition, the generated surface appearance defects and the flash formation at different tool rotation rates were also studied. The model results were validated and compared to the weld appearance, welding defects and the metallurgical zones' shape obtained experimentally.

2. Materials and Procedures

A 3.8 mm thick 1Cr11Ni2W2MoV heat-resistant martensitic stainless-steel plate was used as the starting workpiece material. The chemical composition of the workpiece material is listed in Table 1. The welding tool was made from a W–25%Re refractory material. The FSW tool had a convex scrolled shoulder with a 15 mm shoulder diameter and a threaded tapered pin with a 2.95 mm pin length and 3 mm tip pin diameter. Figure 1 shows a detailed drawing of the FSW tool.

The FSW process consisted of three stages; the plunge, dwell and traverse stages. During the plunge stage, the tool penetrated through the workpiece at a tool rotation rate of 200 rpm and a plunge speed of 60 mm/min. After the tool shoulder reached the predefined plunge depth of 0.3 mm, the tool dwelled for 3 s to heat the tool and the workpiece material. During the traverse stage, the tool traverse speed was kept constant at 75 mm/min, while the tool rotation differed from 250 rpm to 650 rpm. Argon gas shielding was used to prevent surface oxidation. To study the macrostructure, the FSW welded joints were cut perpendicular to the welding direction. The joints' cross-section was ground using SiC paper with a grit size up to 2500 and polished by 1 μm diamond past. Then, the samples were etched in a picral solution (4 g picric acid in 100 mL ethanol) and examined using a Nikon MA200 optical microscope.

Table 1. Chemical composition of 1Cr11Ni2W2MoV steel.

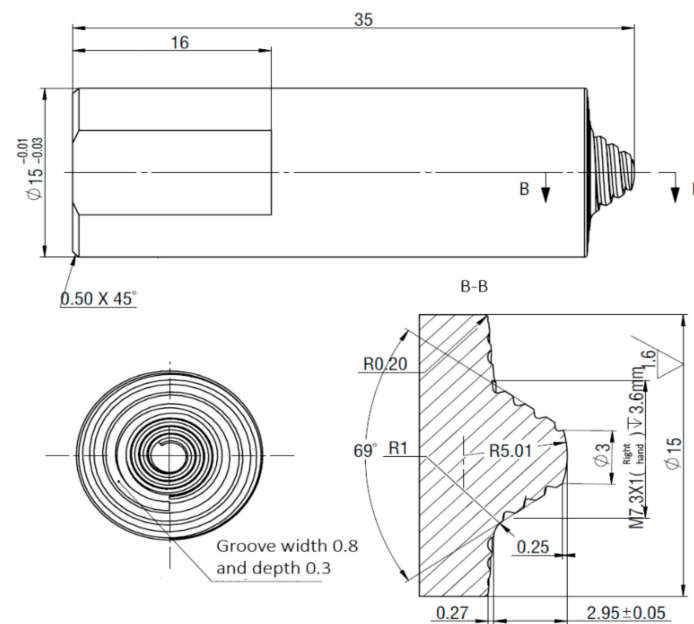| C	Si	Mn	P	S	V	Mo	Ni	Cr	W	Fe
0.12	0.35	0.33	0.025	0.01	0.21	0.41	1.56	11.2	1.56	Bal.

Figure 1. Geometric dimensions of the experimental friction stir welding (FSW) tool.

3. Model Description

A 3D thermo-mechanical finite element model was promoted to anticipate and analyze the plastic strain distribution, temperature distribution and flash formation during the FSW process using the Coupled Eulerian Lagrangian formulation, the Johnson-Cook material low, and coulombs frictional low.

3.1. Governing Equations

In this study, the workpiece domain was modeled as a Eulerian framework, while the welding tool was considered as a Lagrangian rigid body. It is well identified that the conservation equations in the Eulerian description are written using the spatial time derivative. On the contrary, the Lagrangian description for solid and structure analysis conservation equations are a material time derivative. Spatial and material time derivatives can be interconnected with each other as in Equation (1) [33]:

$$D\phi/Dt = \partial\phi/\partial t + v \cdot (\nabla\phi) \tag{1}$$

where ϕ is the arbitrary solution variable, v is the material velocity, and $D\phi/Dt$ and $\partial\phi/\partial t$ are the material and spatial time derivatives of ϕ, respectively.

The mass, momentum, and energy can be written as follows:

$$D\rho/Dt + \rho\nabla \cdot v = 0 \tag{2}$$

$$\rho(Dv/Dt) = \nabla \cdot \sigma + \rho b \tag{3}$$

$$DE/Dt = \nabla \cdot (\sigma \cdot v) + \rho b \cdot v \tag{4}$$

where ρ is the density, σ is the Cauchy stress, b is the body force, and E is the total energy per unit volume.

As the total energy is the sum of kinetic energy ($0.5\rho v \cdot v$) and the internal energy (e), Equation (4) can be rewritten with the velocity strain D as shown in Equation (5):

$$De/Dt = \sigma:D. \tag{5}$$

The three Lagrangian conservation Equations, (2), (3) and (5), can be translated into the spatial time derivative; thus, the Eulerian conservation equations can be written as follows:

$$\partial\rho/\partial t + \nabla \cdot (\rho v) = 0 \tag{6}$$

$$\partial\rho v/\partial t + \nabla \cdot (\rho v \otimes v) = \nabla \cdot \sigma + \rho b \tag{7}$$

$$\partial e/\partial t + \nabla \cdot (ev) = \sigma:D \tag{8}$$

To solve the problem, Equations (6)–(8) can be written in the general conservation form, as shown in Equation (9):

$$\partial\phi/\partial t + \nabla \cdot \mathbf{\Phi}(\phi,v,x,t) = S \tag{9}$$

where **Φ** is the flux function and S is the source term. Operator splitting divides Equation (9) into two equations, as shown in Equations (10) and (11) [34]:

$$\partial\phi/\partial t = S \tag{10}$$

$$\partial\phi/\partial t + \nabla \cdot \mathbf{\Phi}(\phi,v,x,t) = 0 \tag{11}$$

where Equation (10) is referred to as the Lagrangian step, which contains the source term, while Equation (11) is the Eulerian step and contains the convective term.

Figure 2 schematically represents the split operator for each step of the Coupled Eulerian Lagrangian method. Equation (10) corresponds to the standard Lagrangian governing formulation if the spatial time derivative is replaced by the material time derivative on the fixed mesh. In order to solve Equation (11), the deformed mesh is moved to the original one and the volume of the material transported between adjacent elements is calculated. Mass, momentum, energy, and other Lagrangian variables are adapted to account for the material flow between adjacent elements by the transport algorithms.
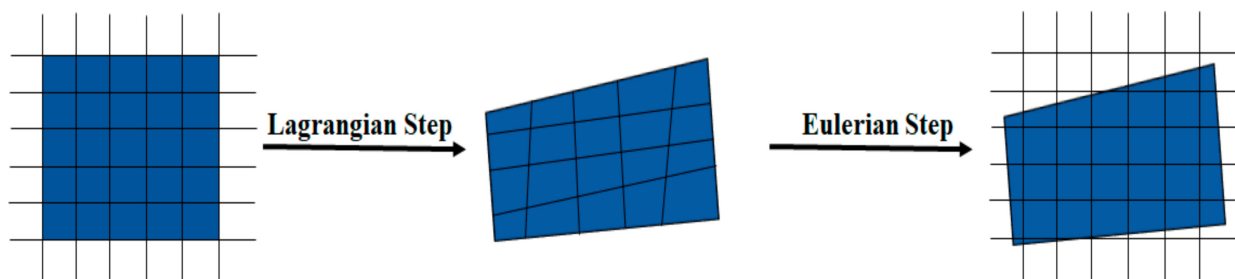

Figure 2. The operator split for the Eulerian formulation.

3.2. Model Geometry and Mesh

The Coupled Eulerian Lagrangian approach was utilized to accomplish the strength of both the Eulerian and Lagrangian methods. The workpiece was modeled as a Eulerian domain, while the Lagrangian formulation was used to consider the welding tool. In order to diminish the computational time (cost), the tool dimensions were the same as the experimental tool but were featureless. However, the featureless tool produces lower equivalent plastic strain and material flow than that produced in experiments using a threaded tool. In addition, the Eulerian domain size used was four times the tool shoulder diameter to realize the accuracy and computational cost [32,35–37]. The Eulerian domain size was $60 \times 60 \times 5.5$ mm^3. As previously stated, the experimental workpiece thickness was 3.8 mm, while the physical workpiece and Eulerian thickness were 4 and 5.5 mm, respectively. The difference between the physical workpiece and the Eulerian domain thicknesses was left unfilled (void) for visualization of flash formation during the FSW process.

The rigid tool was meshed as a four-noded thermally coupled tetrahedron (C3D4T), with a 0.55 mm mesh size and total elements of 36,010, as shown in Figure 3a. The Eulerian domain was sectioned into three parts. The center part, which may contain the processed zone, SZ and thermo-mechanical affected zone (TMAZ), has a fine mesh size, and the side parts have a coarse mesh. An eight-noded thermally coupled linear Eulerian brick (EC3D8RT) was used to mesh the Eulerian domain with 105,600 total number of elements, as is shown in Figure 3b.
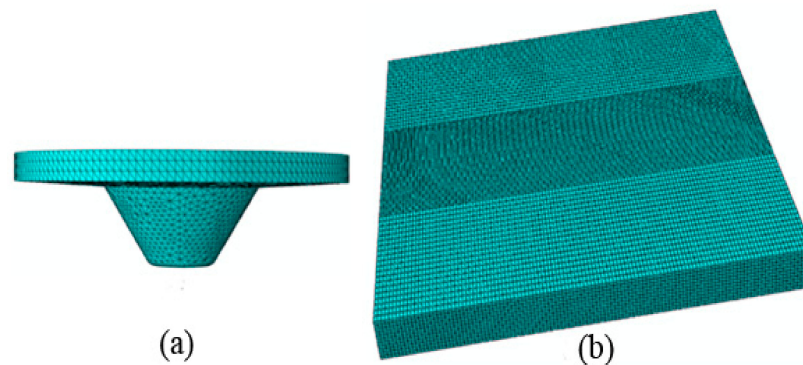

Figure 3. Finite element mesh for tool (**a**) and workpiece (**b**).

3.3. Material Model

The workpiece material during FSW was exposed to a huge strain, ranging from 5 to 80 and a strain rate from 5 to 100 S^1 at elevated temperature, as reported by Kuykendall et al. [38]. The peak temperature can reach 0.9 times the material's melting point. In the present study, the Johnson-Cook material model [39], a temperature and strain rate–dependent visco-plastic model, was used. The yield stress, σ_y, is expressed as:

$$\sigma_y = \left[A + B\left(\varepsilon^n_{pl}\right) \right] \left[1 + C \ln(\frac{\varepsilon_{pl}}{\varepsilon_o}) \right] \left[1 - \left(\frac{T - T_o}{T_{melt} - T_o} \right)^m \right] \tag{12}$$

where A is the material yield stress at room temperature, B is the hardening modulus, n is the work-hardening exponent, C is the strain rate hardening, and m is the thermal softening coefficient. ε^n_{pl}, ε_{pl}, and ε_o are the effective plastic strain, strain rate, and reference strain rate, respectively. T_o and T_{melt} are the ambient temperature and the melting point of the workpiece material, respectively. The Johnson-Cook material constant values are taken from reference [40] and listed in Table 2. Tables 3 and 4 present the workpiece and tool material's mechanical and thermal properties, such as density, elastic modulus, Poisson's ratio, thermal conductivity, and specific heat.

Table 2. Johnson-Cook plasticity model constant for 1Cr11Ni2W2MoV steel [40].

A (MPa)	B (MPa)	C	n	m	T_o	T_{melt}	ε_o
877	621	0.024	0.229	1	25	1450	0.01

Table 3. Physical and mechanical properties of 1Cr11Ni2W2MoV martensitic stainless steel.

	Density (kg/m³)	Yield Strength (MPa)	Thermal Conductivity (W/m·K)	Specific Heat (J/kg·K)	Poisson's Ratio		
	7800	885	20.9	481	0.278		
Young's Modulus (E) VS Temperature (T)							
T (°C)	20	300	400	450	500	550	600
E (MPa)	196,000	172,000	162,000	154,000	142,000	123,000	109,000

Table 4. Physical and mechanical properties of W–25%Re tool material.

Density (kg/m^3)	Yield Strength (MPa)	Thermal Conductivity (W/m·K)	Specific Heat (J/kg·K)	Young's Modulus (MPa)
19,700	1100	35	156	430,000

3.4. Heat Generation and Boundary Conditions

As explained in the introduction, the FSW is a thermo-mechanical process. During FSW, the plastic deformation and friction between the tool and workpiece are two sources of heat [23,41]. The heat generation due to plastic deformation, Q_{pl}, can be calculated using Equation (13):

$$Q_{pl} = \eta \sigma_{fs} \dot{\varepsilon}_{pl} \tag{13}$$

where η is the amount of plastic deformation converted into thermal energy (taken as 90%), $\dot{\varepsilon}_{pl}$ is the plastic strain rate, and σ_{fs} is the flow stress of the workpiece material.

The heat generated from friction can be calculated as follows:

$$Q_f = \tau \gamma \tag{14}$$

where τ is the frictional shear stress and γ is the slip rate.

The frictional shear stress can be calculated according to the classical coulomb's law from Equation (15):

$$\tau = \mu P \tag{15}$$

where μ is the coefficient of friction and P is the contact pressure. For FSW, the coefficient of friction is a function of contact pressure P, slip rate (γ), and temperature. However, accurate values for the friction coefficient during FSW cannot be determined because of the process complexity [42]. Subsequently, a constant coefficient of friction values is used. Ahmed et al. [43] took the friction coefficient of 0.3 in their simulation work of FSW of low alloy steel, while Nandan et al. [44] used a coefficient of friction equal to 0.4 to simulate the FSW of 304 austenitic stainless steel. Therefore, a constant coefficient of friction of 0.35 is considered in this investigation.

In this study, the heat loss due to conductance between the workpiece bottom surface and the backing plate is taken into consideration as the main source of heat loss, while the heat loss from other surfaces to the surrounding environment is neglected. A constant convection coefficient at the workpiece bottom surface of 3000 W/m^2·K is assumed instead of the backing plate. Almoussawi et al. [24] and Ahmed et al. [43] assumed a convection coefficient of 2000 W/m^2·K at the bottom surface, and Chauhan et al. [45] defined it as 4000 W/M^2·K. In order to prohibit the material flow out of the Eulerian domain, a velocity boundary condition is applied as shown schematically in Figure 4. As in the experimental work, the simulation work consists of three stages: the plunge, dwell, and traverse stages. In addition, the position control method is applied in the tool to achieve a tool shoulder plunge depth of 0.3 mm. After reaching the predefined plunge depth, the tool dwells for 3 s to heat the tool and workpiece before the traverse stage.
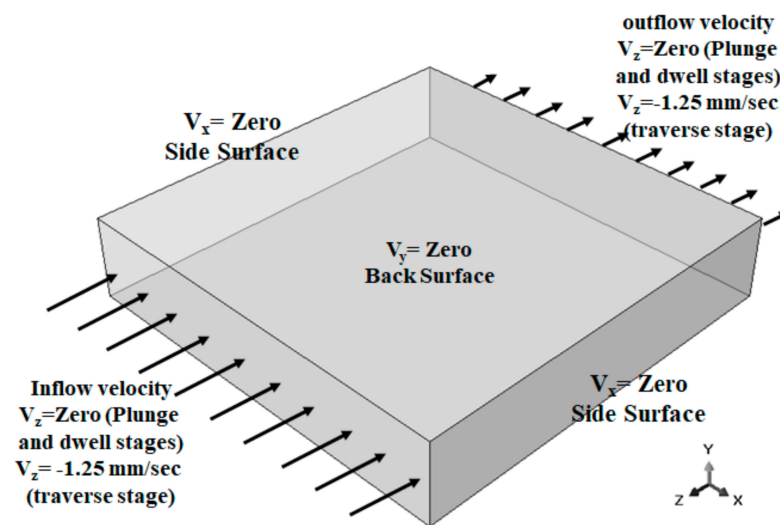
Figure 4. Velocity boundary conditions.

4. Results and Discussion

4.1. Plunge and Dwell Stages

Figure 5 shows the temperature distribution in both the plunge and dwell stages at the top surface and weld cross section. As there is no traverse movement, the temperature in the plunge and dwell stages was uniformly distributed, as demonstrated in the top and cross section views. As indicated previously, the tool dwells during the dwell stage to heat the tool and workpiece material. As a result, the peak temperature in the dwell stage is higher than that in the plunge stage. The temperature spreads over a wide area in the dwell stage. The peak temperature in the plunge stage is about 850 °C and lies under the tool shoulder, while the peak temperature during the dwell stage reaches 1120 °C and lies near the shoulder-pin intersection point.
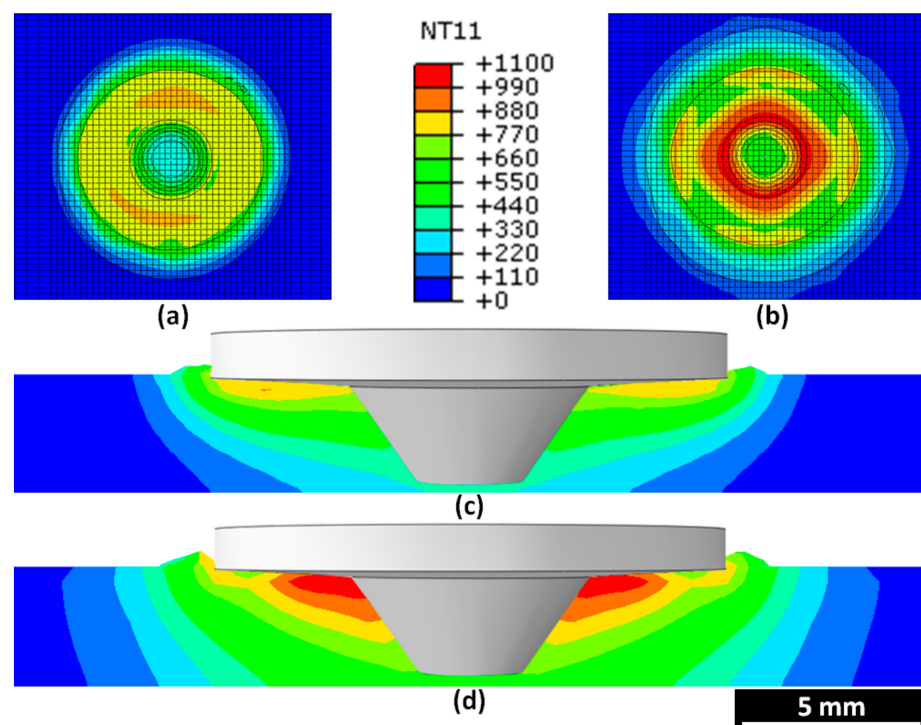

Figure 5. Temperature distribution in °C at plunge and dwell stages. (**a**) Top view at plunge, (**b**) top view at dwell, (**c**) cross section view at plunge, and (**d**) cross section view at dwell.

A uniform flash is formed at the external edges of the joint. It is obvious from Figure 5c,d that the flash in the dwell stage is thicker due to the higher peak temperature and plastic deformation. Dialami et al. [46] reported that increasing the welding peak temperature resulted in flash formation. In the same way, Kim et al. [47] showed that the higher heat generated under the tool shoulder softens the material and expels it out by the tool pressure in the form of flash.

Figure 6 presents the equivalent plastic strain, showing the top and cross section views, in the plunge and dwell stages. As exhibited in Figure 6c,d, the plastic strain distribution in both stages is symmetrical around the weld center. However, the equivalent plastic strain in the dwell stage is higher. The higher equivalent plastic strain value can be found near the shoulder-pin intersection point, as in the temperature distribution, in both stages; it decreases toward the tool shoulder and pin tip. This may be attributed to the severe plastic deformation near the shoulder-pin intersection point, caused by both the tool pin and shoulder.
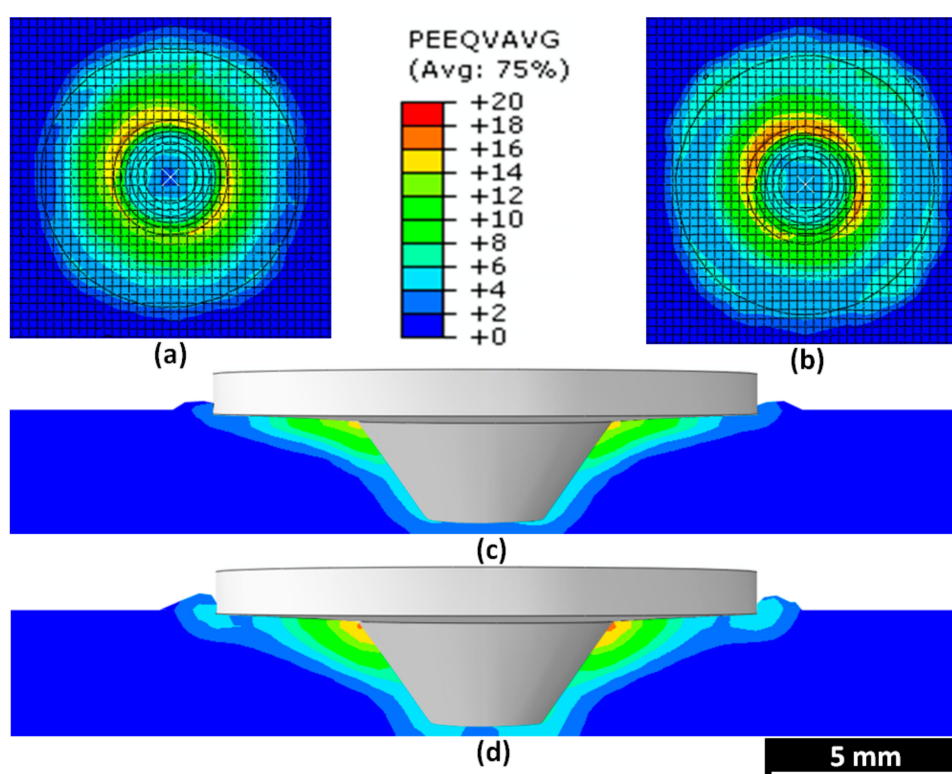

Figure 6. Equivalent plastic strain distribution at plunge and dwell stages. (**a**) Top view at plunge, (**b**) top view at dwell, (**c**) cross section view at plunge, and (**d**) cross section view at dwell.

4.2. Traverse Stage and Model Validation

4.2.1. Temperature Distribution and Plastic Strain

Experimental and simulation work are conducted using five different tool rotations: 250, 350, 450, 550 and 650 rpm. Figures 7–10 show the experimental macrostructures for all welded conditions and the corresponding temperature distribution (Node Temperature NT) and equivalent plastic strain (PEEQVAVG) results from the CEL model. For all tool rotations, the higher peak temperatures are found in the SZ, with slightly higher values at the retreating side (RS). Sorger et al. [48] used FSW to join DH36 steel and reported that the peak temperature was found near the FSW tool, i.e., inside the SZ. In addition, the temperatures measured at the RS were higher than the temperatures measured at the advancing side (AS) by 25 °C [48]. The peak temperature increases with an increase in

the tool rotation rate. At the SZ of joints welded at 250, 350, 450 and 550 rpm, the peak temperatures are 1128, 1181, 1254 and 1300 °C, respectively.
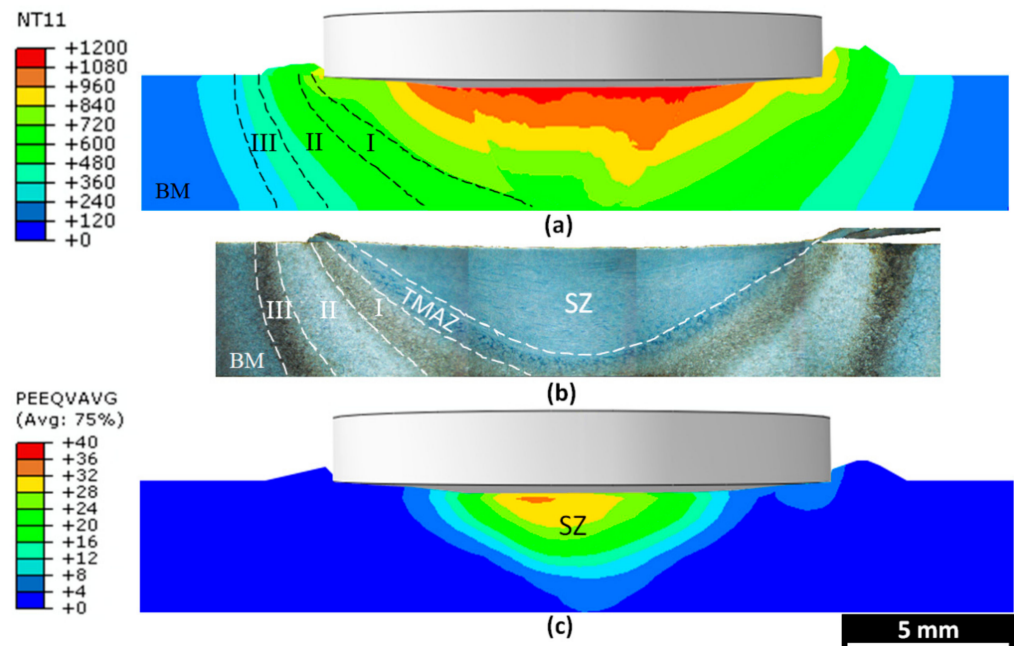
Figure 7. Temperature and equivalent plastic strain distribution of welded joint at 250 rpm: (**a**) temperature distribution in °C, (**b**) experimental macrograph, and (**c**) equivalent plastic strain distribution. (AS on the left, counter-clockwise tool rotation).

Figure 8. Temperature and equivalent plastic strain distribution of welded joint at 350 rpm: (**a**) temperature distribution in °C, (**b**) experimental macrograph, and (**c**) equivalent plastic strain distribution. (AS on the left, counter-clockwise tool rotation).
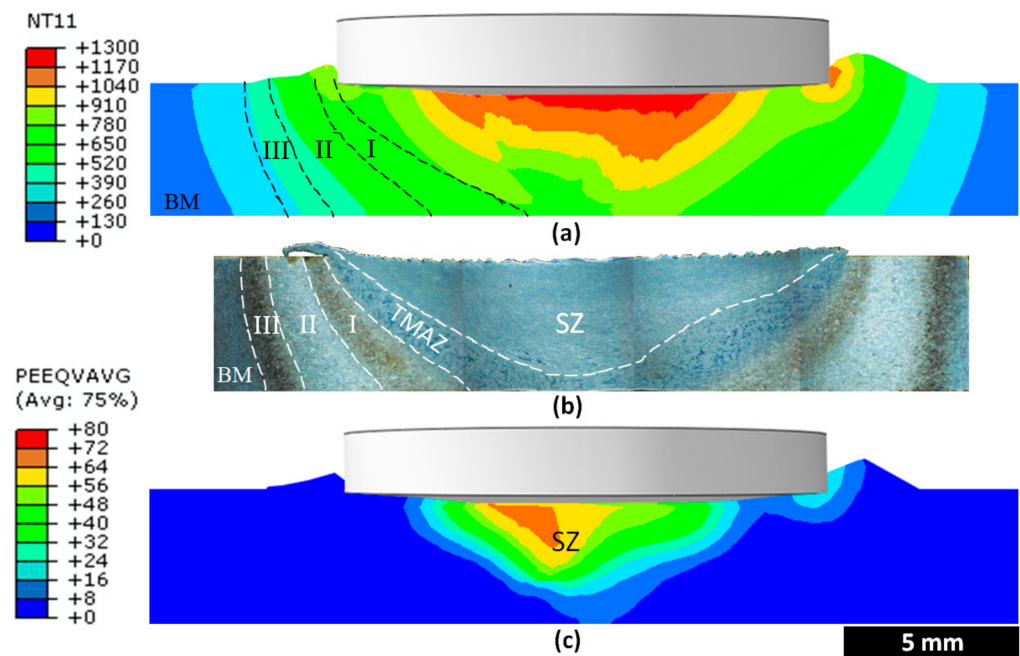
Figure 9. Temperature and equivalent plastic strain distribution of welded joint at 450 rpm:(**a**) temperature distribution in °C, (**b**) experimental macrograph, and (**c**) equivalent plastic strain distribution. (AS on the left, counter-clockwise tool rotation).
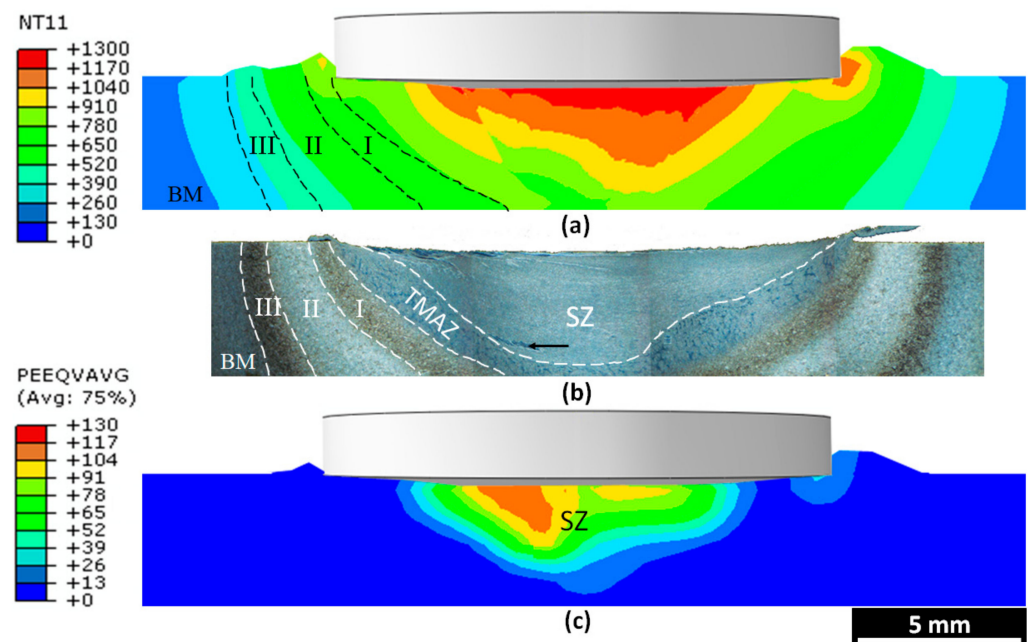

Figure 10. Temperature and equivalent plastic strain distribution of welded joint at 550 rpm: (**a**) temperature distribution in °C, (**b**) experimental macrograph, and (**c**) equivalent plastic strain distribution. (AS on the left, counter-clockwise tool rotation).
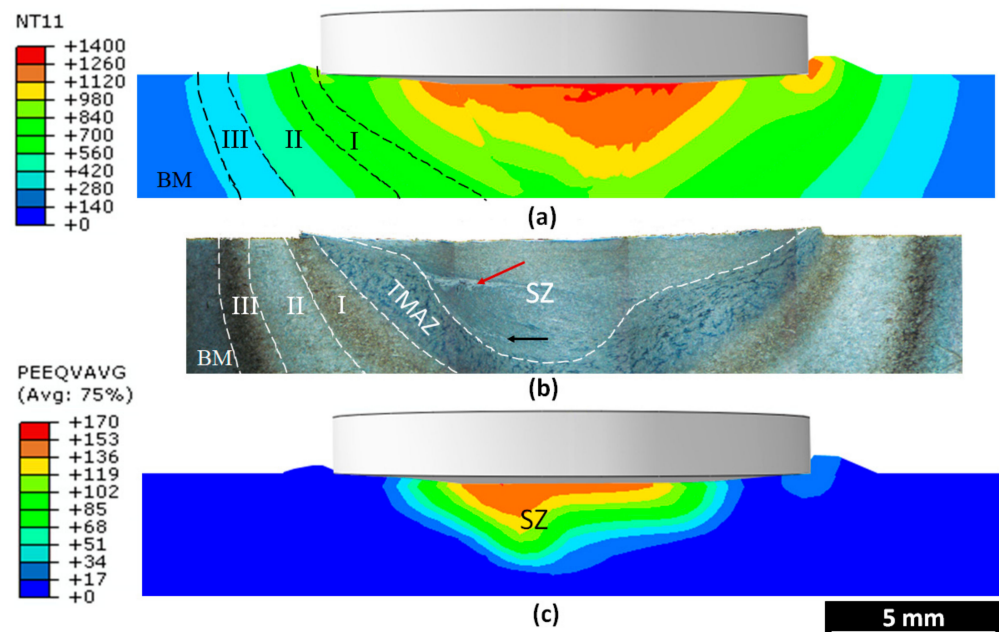
The experimental weld cross section is characterized by four metallurgical zones, including the base metal (BM), HAZ, thermo-mechanical affected zone (TMAZ) and SZ. The HAZ can be divided into three zones—HAZI, II and III—according to their color under etching and temperature distribution. To understand the difference between the three HAZs, the thermal cycles are recorded for the three HAZs in the AS and RS. Figure 11 shows the location of the selected nodal points in each zone.
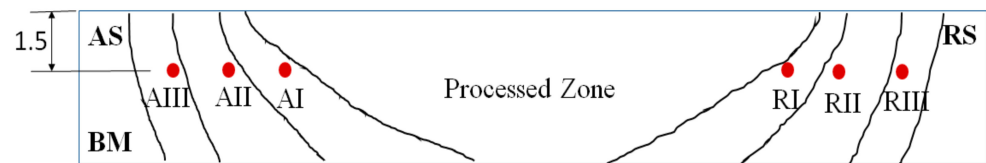
Figure 11. Schematic location of nodes on the weld cross section for measuring the thermal cycle.

Figures 12 and 13 exhibit the thermal cycles at the selected nodal points in Figure 11 for the joints welded at 250 and 550 rpm, respectively. As the plunge and dwell stages are the same for all welds, the thermal cycles until the dwell stage, i.e., until the second 6.25, for all respective points are nearly the same. The peak temperatures in the RS are slightly higher than those in the AS. In addition, the cooling rate in the RS is slower than the cooling rate in the AS.
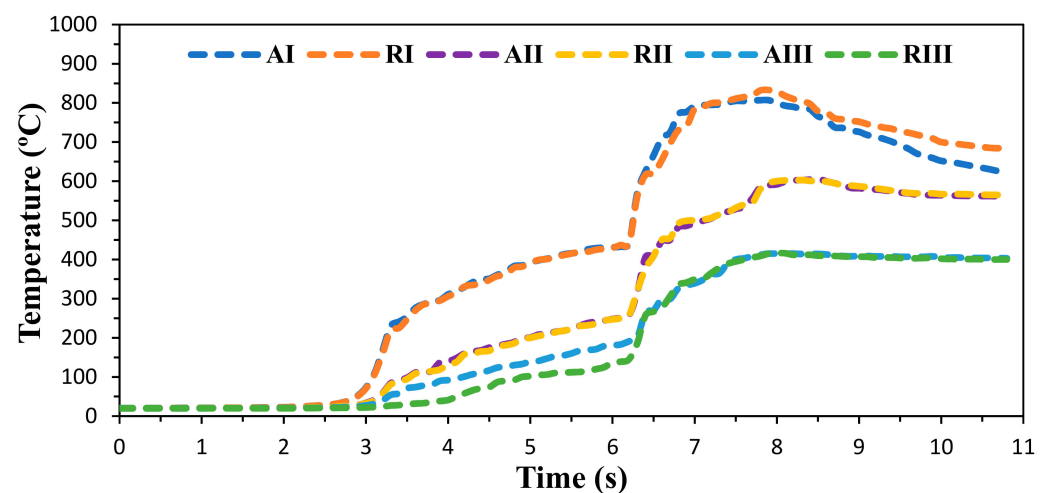

Figure 12. Heat affected zone's (HAZ) thermal cycle for the FSW welded joint at 250 rpm.
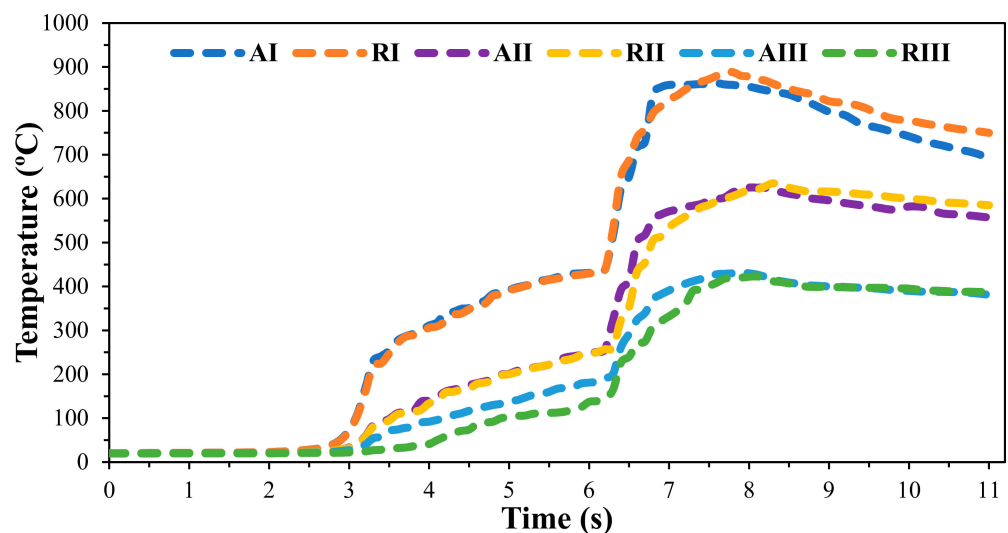
Figure 13. Heat affected zone's (HAZ) thermal cycle for the FSW welded joint at 550 rpm.

For the joint welded at 250 rpm, the peak temperatures at HAZI, II and III are 830, 600 and 415 °C, respectively. Likewise, the peak temperatures at the same HAZs in the joint welded at 550 rpm are 880, 635 and 423 °C. Lu et al. [49] studied the effect of tempering temperature on the microstructure of 13 wt. % Cr- type martensitic stainless steel. They reported that the resultant microstructure of the sample tempered at 300 °C is tempered

martensite and Cr-rich $M_{23}C_6$ carbides. The number of $M_{23}C_6$ carbides increased with an increase in the tempering temperature [49]. It is clear from these results and data that HAZI reaches the intermediate temperature between A_1 and A_3, while HAZII and III are tempered at high temperature and low temperature, respectively. Moreover, the HAZ width in both experimental and simulation work increased with increasing the tool rotation. The same result was reported by Iqbal et al. [50]. The increase in the tool rotation softens the material because of the high heat generated and bolsters the extending of the heat removal across the workpiece.

Figure 7b,c show that the SZ has a basin-like shape that is symmetric across the weld centerline in both experimental and computed results. However, with an increase in the tool rotations (Figure 8b,c, Figure 9b,c, Figure 10b,c), the SZ at the RS takes a wavy shape. This may be attributed to the higher shear stress at the AS compared to the RS. At the highest tool rotation, the sample has a more complex material flow. In addition, the equivalent plastic strain increases with an increase in the tool rotation. Increasing the tool rotations enhances the tangential velocity around the pin, leading to a higher deformation rate, or in other words, a higher strain rate. Compared to the AS, the plastic strain at the tool shoulder edge in the RS is high. This may be attributed to the excessive flash formed at the RS.

It is evident that there are no volumetric defects in the cross section of the welds, except the band structure shown in Figures 9b and 10b. The band structure at the bottom AS shown in Figures 9b and 10b, specified by black arrows, may be due to the tool pin tip wear at high tool rotation rates. In addition to the tool wear, the peak temperature at the SZ of the sample welded at 550 rpm is higher than 1300 °C. Below this temperature, the delta ferrite phase forms, according to Sam et al. [51]. The delta ferrite does not transform to austenite and then martensite during the cooling process because of the high cooling rate. Therefore, it is expected that the clear band structure at the top AS, specified by the red arrow in Figure 10b, is due to the tool wear and the delta ferrite phase formed at high temperature. Good agreement between the computed results and the experimental results indicates that the model can be utilized to estimate the thermal cycles and weld macrostructure at different welding conditions.

4.2.2. Weld Appearance and Defects

Figure 14a–e shows the surface appearance and flash formed for all joints from FSW experiments and modeling results using EVF-VOID. EVF-VOID is the volume fraction of the empty regions in a Eulerian domain. An EVF = 1 indicates that the element is empty, while EVF = zero indicates that the element is completely filled with the material instance. No surface defects, i.e., grooves and/or lack of fill, appear on the weld surface of all samples, except the sample welded at 650 rpm. Samples welded at 250 and 350 rpm have a good surface appearance and a uniform surface ripple, as can be seen in Figure 14a,b, respectively. The surface roughness increases with an increase in the tool rotation rate, and the ripples become deeper and discontinuous, as exhibited in Figure 14c,d. The black ellipse in Figure 14b–d refers to the rough surface at the high tool rotation rates. Iqbal et al. [50] reported that a smooth weld appearance with fine ripples was produced at 800 rpm, while increasing the tool rotation to 1500 rpm resulted in a rough surface and non-uniform ripples [50]. In addition, the weld surface color of the sample welded at 550 rpm shows that the weld surface is overheated. This agrees with the temperature distribution for the same sample shown in Figure 10a. The sample surface temperature exceeds 1300 °C. This temperature is more than 90% of the workpiece material melting point. As the tool rotation increases (650 rpm), i.e., the welding temperature increases, the steel may begin to show a tendency toward decohesion at the weld surface. At this point, the tool shoulder is insufficient to constrain and form the plasticized weld metal. Some loss of material will occur, either in the form of weld flash or in excessive positive reinforcement of the weld surface. The result is a lack of material to flow completely behind the tool from the retreating side to the advancing side of the weld, as shown in Figure 14e.
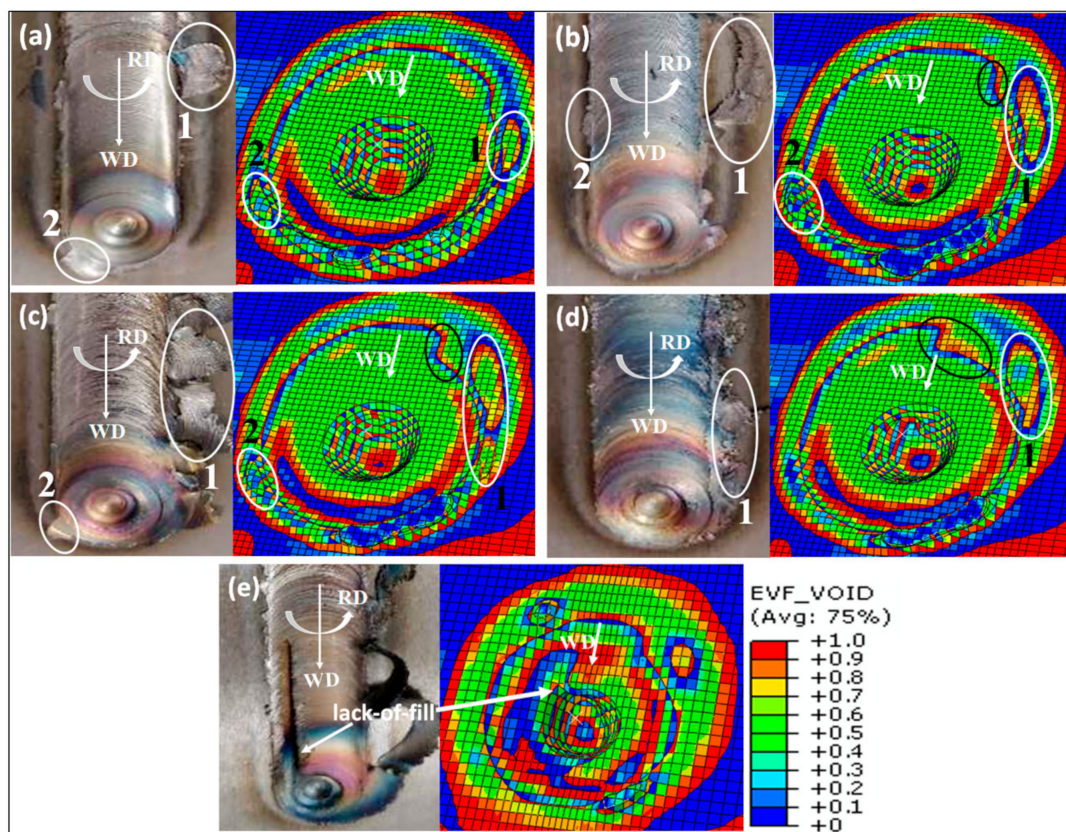
Figure 14. Visualization of the generated flash and weld surface appearance experimentally and numerically using EVF-VOID for samples welded at (**a**) 250 rpm, (**b**) 350 rpm, (**c**) 450 rpm, (**d**) 550 rpm, and (**e**) 650 rpm.

A little flash is formed at the lowest tool rotation, i.e., 250 rpm, in both experimental and computed results. The flash size increases with increasing the tool rotation rate. The increase in the tool rotation rate enhances the heat generated during the FSW process. As explained earlier, the increased heat input leads to more plasticized material. The softened material splits under the tool pressure out in the form of flash [52]. Furthermore, for all welding conditions, most of the flash is formed in the RS indicated by the white ellipse numbered 1 in Figure 14a–d. On the other hand, no or little flash is formed in the AS indicated by the white ellipse numbered 2 in Figure 14a–d. During the traverse stage, the material from the leading edge is continuously softened and streams to the trailing edge through the RS. If the material under the tool shoulder is dramatically plasticized, the material spews out from the weld cavity forming the flash in the RS [53]. The traverse stage of the numerical work is shorter than that of the experimental work in order to reduce the computational cost; there was no remarkable change when using a longer time for one sample.

Figure 15a–e shows the computed weld side view at different tool rotation rates. No volumetric defects occur with increasing the tool rotation up to 550 rpm. However, a small void initiation can be observed at 550 rpm (Figure 15d). Such a defect did not appear in the experiment due to the fixed coefficient of friction and featureless tool geometry used in the model. By increasing the tool rotation to 650 rpm, a lack-of-fill defect is produced, as shown in Figure 15e. Figures 14 and 15 indicate that the weld surface appearance and generated defects of the computed results agreed well with the experimental ones.
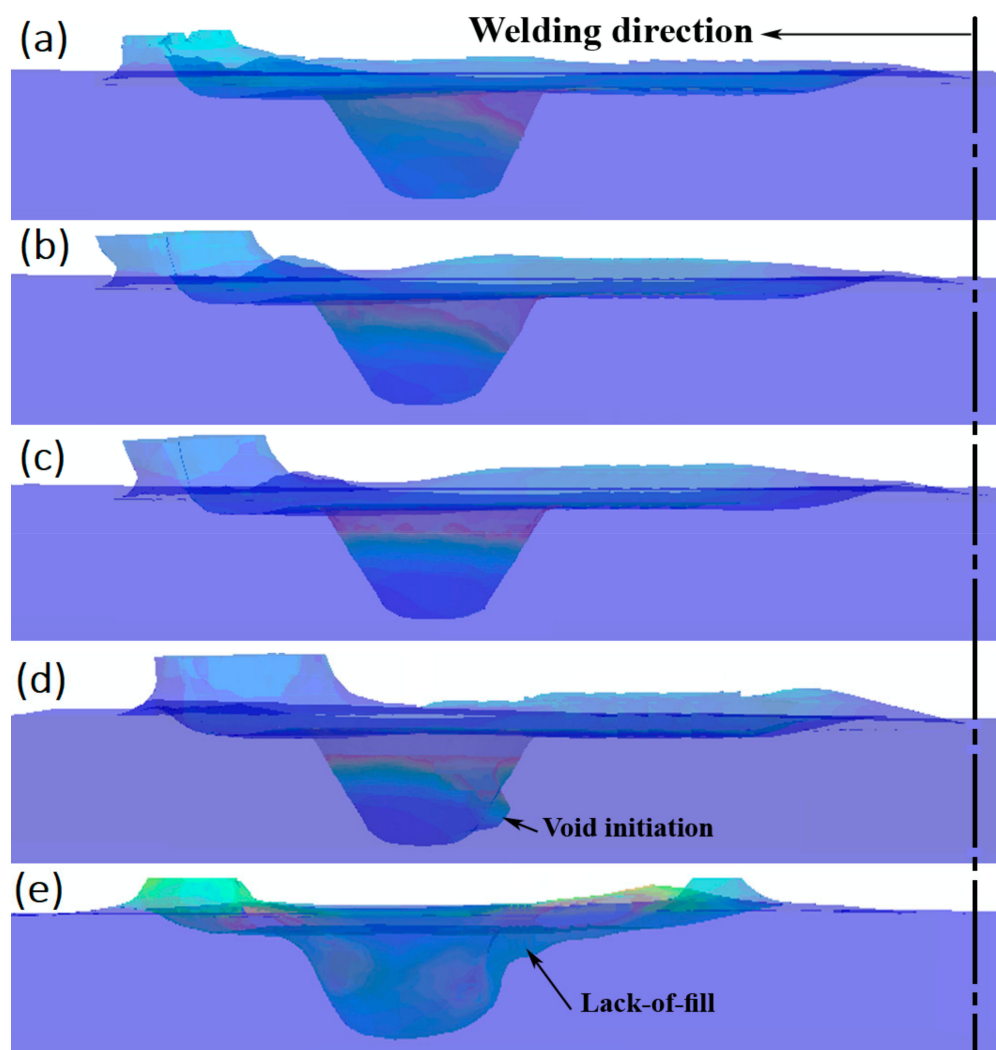
Figure 15. Equivalent plastic strain and defects visualization at various welding conditions: (**a**) 250 rpm, (**b**) 350 rpm, (**c**) 450 rpm, (**d**) 550 rpm, and (**e**) 650 rpm.

5. Conclusions

A three-dimensional Coupled Eulerian Lagrangian model was developed using Abaqus/Explicit to simulate the FSW of 1Cr11Ni2W2MoV heat-resistant martensitic stainless steel. All the three stages of the FSW process, i.e., plunge, dwell and traverse, were studied. The temperature distribution, plastic strain and weld appearance at different tool rotation rates were investigated. The following conclusions can be drawn:

1. During the plunge and dwell stages, as there is no traverse motion, a uniform flash is formed at the outer tool edges. Compared to the plunge stage, the workpiece is more heated and plasticized after the dwell stage.
2. A basin-like shaped stir zone is created at the different tool rotation rates. However, the increase in the tool rotation rate to more than 350 rpm leads to an asymmetric stir zone around the weld centerline. The equivalent plastic strain is increased dramatically with an increase in the tool rotation.
3. The peak temperature is increased with an increase in the tool rotation. The peak temperature at 550 rpm reaches the austenite-to-delta ferrite transformation temperature. The HAZ width increases with an increase in the tool rotation. Moreover, the HAZ is divided into three zones according to the thermal cycles and the experimental macrostructure.

4. A fine weld surface roughness is achieved at low tool rotation, i.e., 250 and 350 rpm. The major flash is formed at the RS for all joints and increases with the tool rotation. At 650 rpm, a lack-of-fill defect is observed at the advancing side of the SZ.

5. The processed zone shape, HAZs and weld appearance computed numerically at different tool rotations are in good agreement with the experimental results. Thus, the model is capable of studying various process parameters, such as low-temperature conditions, which are expected to reduce the HAZ width.

Author Contributions: Conceptualization and design of experiment, M.R. and H.L.; experiment, validation, and formal analysis, M.R.; project administration, H.L.; software, M.R. and M.M.Z.A.; writing—original draft preparation, M.R.; writing—review and editing, M.R., H.L. and M.M.Z.A.; supervision, H.L. and G.-J.Y. All authors have read and agreed to the published version of the manuscript.

Institutional Review Board Statement: Not applicable.

Informed Consent Statement: Not applicable.

Conflicts of Interest: The authors declare no conflict of interest.

References

1. Kunrong, J.; Zhufeng, Y. Testing study on low cycle fatigue of 1Cr11Ni2W2MoV steel welding joint at middle temperatur. *J. Xian Polytech. Univ.* **2009**, *23*, 48–52.
2. Hong, Y.; Jinxue, W.; Huai, Y.; Guodong, Z. Microstructure and mechanical properties of flash butt welded joints of 1Cr11Ni2W2MoV stainless steel after different heat treatment. *Electr. Weld. Mach.* **2017**, *47*, 52–54.
3. Zhang, C.; Li, M.Q.; Li, H. On the shear strength of similar diffusion bonded 1Cr11Ni2W2MoV stainless steel hollow structural components: Effect of void morphology. *J. Manuf. Process.* **2017**, *29*, 10–17. [CrossRef]
4. Thomas, W.M.; Nicholas, E.D.; Needham, J.C.; Murch, M.G.; Templesmith, P.; Dawes, C.J. Friction Stir Butt Welding: International. GB Patent Application no. 9125978.8, 8 December 1991.
5. Tiwari, A.; Pankaj, P.; Biswas, P.; Kore, S.D.; Rao, A.G. Tool performance evaluation of friction stir welded shipbuilding grade DH36 steel butt joints. *Int. J. Adv. Manuf. Technol.* **2019**, *103*, 1989–2005. [CrossRef]
6. Meyghani, B.; Awang, M. A Comparison Between the Flat and the Curved Friction Stir Welding (FSW) Thermomechanical Behaviour. *Arch. Comput. Methods Eng.* **2020**, *27*, 563–576. [CrossRef]
7. Mishra, R.S.; Ma, Z.Y. Friction stir welding and processing. *Mater. Sci. Eng. R Rep.* **2005**, *50*, 1–78. [CrossRef]
8. Kim, H.; Lee, K.; Kim, J.; Lee, C.; Jung, Y.; Kang, S. A Study on the Friction Stir Welding Experiment and Simulation of the Fillet Joint of Extruded Aluminum Material of Electric Vehicle Frame. *Appl. Sci.* **2020**, *10*, 9103. [CrossRef]
9. Kang, S.; Kim, J.; Jang, Y.; Lee, K. Welding Deformation Analysis, Using an Inherent Strain Method for Friction Stir Welded Electric Vehicle Aluminum Battery Housing, Considering Productivity. *Appl. Sci.* **2019**, *9*, 3848. [CrossRef]
10. Kayode, O.; Akinlabi, E.T. An overview on joining of aluminium and magnesium alloys using friction stir welding (FSW) for automotive lightweight applications. *Proc. Mater. Res. Express* **2019**, *6*, 112005. [CrossRef]
11. Ahmed, M.M.Z.; Ataya, S.; El-Sayed Seleman, M.M.; Mahdy, A.; Alsaleh, N.A.; Ahmed, E. Heat Input and Mechanical Properties Investigation of Friction Stir Welded AA5083/AA5754 and AA5083/AA7020. *Metals* **2021**, *11*, 68. [CrossRef]
12. Kusuda, Y. Honda develops robotized FSW technology to weld steel and aluminum and applied it to a mass-production vehicle. *Ind. Rob.* **2013**, *40*, 208–212. [CrossRef]
13. Güleryüz, G. Relationship between FSW parameters and hardness of the ferritic steel joints: Modeling and optimization. *Vacuum* **2020**, *178*, 109449. [CrossRef]
14. Matlan, M.J.B.; Mohebbi, H.; Pedapati, S.R.; Awang, M.B.; Ismail, M.C.; Kakooei, S.; Dan, N.E. Dissimilar friction stir welding of carbon steel and stainless steel: Some observation on microstructural evolution and stress corrosion cracking performance. *Trans. Indian Inst. Met.* **2018**, *71*, 2553–2564. [CrossRef]
15. Sun, Y.; Fujii, H.; Morisada, Y. Double-sided friction stir welding of 40 mm thick low carbon steel plates using a pcBN rotating tool. *J. Manuf. Process.* **2020**, *50*, 319–328. [CrossRef]
16. Acevedo, J.L.; Morales, C.E.; Rodriguez, B.R.; Cerna, P.B. Microstructural and mechanical behavior study of 5052 aluminum alloy welded by FSW process. *MRS Adv.* **2019**, *4*, 3041–3052. [CrossRef]
17. Tiwari, A.; Singh, P.; Pankaj, P.; Biswas, P.; Kore, S.D. FSW of low carbon steel using tungsten carbide (WC-10wt.%Co) based tool material. *J. Mech. Sci. Technol.* **2019**, *33*, 4931–4938. [CrossRef]
18. He, B.; Cui, L.; Wang, D.; Liu, Y.; Liu, C.; Li, H. The metallurgical bonding and high temperature tensile behaviors of 9Cr-1W steel and 316L steel dissimilar joint by friction stir welding. *J. Manuf. Process.* **2019**, *44*, 241–251. [CrossRef]
19. Ahmed, M.M.Z.; Barakat, W.S.; YA Mohamed, A.; A Alsaleh, N.; Elkady, O.A. The Development of WC-Based Composite Tools for Friction Stir Welding of High-Softening-Temperature Materials. *Metals* **2021**, *11*, 285. [CrossRef]

20. Ahmed, M.M.Z.; Seleman, M.M.E.-S.; Shazly, M.; Attallah, M.M.; Ahmed, E. Microstructural development and mechanical properties of friction stir welded ferritic stainless steel AISI 409. *J. Mater. Eng. Perform.* **2019**, *28*, 6391–6406. [CrossRef]

21. Yang, C.; Dou, W.; Pittman, C.C.; Zhou, E.; Xu, D.; Li, H.; Lekbach, Y.; Wang, F. Microbiologically influenced corrosion behavior of friction stir welded S32654 super austenitic stainless steel in the presence of Acidithiobacillus caldus SM-1 biofilm. *Mater. Today Commun.* **2020**, *25*, 101491. [CrossRef]

22. Da Silva, Y.C.; Júnior, F.J.V.O.; dos Santos, J.F.; Marcondes, F.; Silva, C. Numerical investigation of the influence of FSW parameters on the heat and mass transfer of austenitic stainless steels. *Weld. World* **2020**, *64*, 2019–2032. [CrossRef]

23. Zhu, Z.; Wang, M.; Zhang, H.; Zhang, X.; Yu, T.; Wu, Z. A finite element model to simulate defect formation during friction stir welding. *Metals* **2017**, *7*, 256. [CrossRef]

24. Al-moussawi, M.; Smith, A.J.; Young, A.; Cater, S.; Faraji, M. Modelling of friction stir welding of DH36 steel. *Int. J. Adv. Manuf. Technol.* **2017**, *92*, 341–360. [CrossRef]

25. Colegrove, P.A.; Shercliff, H.R. Development of Trivex friction stir welding tool Part 2–three-dimensional flow modelling. *Sci. Technol. Weld. Join.* **2004**, *9*, 352–361. [CrossRef]

26. Kim, S.-D.; Yoon, J.-Y.; Na, S.-J. A study on the characteristics of FSW tool shapes based on CFD analysis. *Weld. World* **2017**, *61*, 915–926. [CrossRef]

27. Zhu, Y.; Chen, G.; Zhang, S.; Cheng, Q.; Zhang, G.; Shi, Q. Numerical simulation of material flow during FSW to predict defect generation based on non-uniform tool–material contact condition. In Proceedings of the 8th International Conference on Physical and Numerical Simulation of Materials Processing (ICPNS), Seattle, WA, USA, 14–17 October 2016.

28. Meyghani, B.; Awang, M.B.; Emamian, S.S.; Mohd Nor, M.K.B.; Pedapati, S.R. A comparison of different finite element methods in the thermal analysis of friction stir welding (FSW). *Metals* **2017**, *7*, 450. [CrossRef]

29. Guerdoux, S.; Fourment, L. A 3D numerical simulation of different phases of friction stir welding. *Model. Simul. Mater. Sci. Eng.* **2009**, *17*, 75001. [CrossRef]

30. Fourment, L.; Gastebois, S.; Dubourg, L. Calibration of 3D ALE finite element model from experiments on friction stir welding of lap joints. *AIP Conf. Proc.* **2016**, *1769*, 100006.

31. Meyghani, B.; Awang, M.B.; Wu, C.S. Thermal analysis of friction stir processing (FSP) using arbitrary Lagrangian-Eulerian (ALE) and smoothed particle hydrodynamics (SPH) meshing techniques. *Materwiss. Werksttech.* **2020**, *51*, 550–557. [CrossRef]

32. Ansari, M.A.; Samanta, A.; Behnagh, R.A.; Ding, H. An efficient coupled Eulerian-Lagrangian finite element model for friction stir processing. *Int. J. Adv. Manuf. Technol.* **2019**, *101*, 1495–1508. [CrossRef]

33. Benson, D.J.; Okazawa, S. Contact in a multi-material Eulerian finite element formulation. *Comput. Methods Appl. Mech. Eng.* **2004**, *193*, 4277–4298. [CrossRef]

34. Benson, D.J. A mixture theory for contact in multi-material Eulerian formulations. *Comput. Methods Appl. Mech. Eng.* **1997**, *140*, 59–86. [CrossRef]

35. Zhang, Z.; Zhang, H.W. Numerical studies on controlling of process parameters in friction stir welding. *J. Mater. Process. Technol.* **2009**, *209*, 241–270. [CrossRef]

36. Al-Badour, F.; Merah, N.; Shuaib, A.; Bazoune, A. Coupled Eulerian Lagrangian finite element modeling of friction stir welding processes. *J. Mater. Process. Technol.* **2013**, *213*, 1433–1439. [CrossRef]

37. Schmidt, H.; Hattel, J.; Wert, J. An analytical model for the heat generation in friction stir welding. *Model. Simul. Mater. Sci. Eng.* **2003**, *12*, 143. [CrossRef]

38. Kuykendall, K.; Nelson, T.; Sorensen, C. On the selection of constitutive laws used in modeling friction stir welding. *Int. J. Mach. Tools Manuf.* **2013**, *74*, 74–85. [CrossRef]

39. Johnson, G.R.; Cook, W.H. A constitutive model and data for metals subjected to large strains, high strain rates and high temperatures. In Proceedings of the 7th International Symposium on Ballistics, The Hague, The Netherlands, 19–21 April 1983; pp. 541–547.

40. Zhi-qiang, F.; Zhi-xian, Q.; Tao, J.; De-ping, G. Experimental Study of 1CrllNi2W2MoV Under Tensile Impact. In Proceedings of the Material Defense Engineering, Proceedings of the 13th Symposium on Engine Structure and Vibration, Stuttgart, Germany, 19–22 September 2006; pp. 259–262.

41. Zahmatkesh, B.; Enayati, M.H.; Karimzadeh, F. Tribological and microstructural evaluation of friction stir processed Al2024 alloy. *Mater. Des.* **2010**, *31*, 4891–4896. [CrossRef]

42. Nandan, R.; DebRoy, T.; Bhadeshia, H. Recent advances in friction-stir welding–process, weldment structure and properties. *Prog. Mater. Sci.* **2008**, *53*, 980–1023. [CrossRef]

43. Ahmad, B.; Galloway, A.; Toumpis, A. Advanced numerical modelling of friction stir welded low alloy steel. *J. Manuf. Process.* **2018**, *34*, 625–636. [CrossRef]

44. Nandan, R.; Roy, G.G.; Lienert, T.J.; DebRoy, T. Numerical modelling of 3D plastic flow and heat transfer during friction stir welding of stainless steel. *Sci. Technol. Weld. Join.* **2006**, *11*, 526–537. [CrossRef]

45. Chauhan, P.; Jain, R.; Pal, S.K.; Singh, S.B. Modeling of defects in friction stir welding using coupled Eulerian and Lagrangian method. *J. Manuf. Process.* **2018**, *34*, 158–166. [CrossRef]

46. Dialami, N.; Cervera, M.; Chiumenti, M. Defect formation and material flow in Friction Stir Welding. *Eur. J. Mech.* **2020**, *80*, 103912. [CrossRef]

47. Kim, Y.G.; Fujii, H.; Tsumura, T.; Komazaki, T.; Nakata, K. Effect of welding parameters on microstructure in the stir zone of FSW joints of aluminum die casting alloy. *Mater. Lett.* **2006**, *60*, 3830–3837. [CrossRef]

48. Sorger, G.; Sarikka, T.; Vilaça, P.; Santos, T.G. Effect of processing temperatures on the properties of a high-strength steel welded by FSW. *Weld. World* **2018**, *62*, 1173–1185. [CrossRef]

49. Lu, S.-Y.; Yao, K.-F.; Chen, Y.-B.; Wang, M.-H.; Liu, X.; Ge, X. The effect of tempering temperature on the microstructure and electrochemical properties of a 13wt.% Cr-type martensitic stainless steel. *Electrochim. Acta* **2015**, *165*, 45–55. [CrossRef]

50. Iqbal, Z.; Bazoune, A.; Al-Badour, F.; Shuaib, A.; Merah, N. Effect of tool rotational speed on friction stir welding of ASTM A516-70 Steel Using W–25% Re Alloy tool. *Arab. J. Sci. Eng.* **2019**, *44*, 1233–1242. [CrossRef]

51. Sam, S.; Das, C.R.; Ramasubbu, V.; Albert, S.K.; Bhaduri, A.K.; Jayakumar, T.; Kumar, E.R. Delta ferrite in the weld metal of reduced activation ferritic martensitic steel. *J. Nucl. Mater.* **2014**, *455*, 343–348. [CrossRef]

52. Tamadon, A.; Baghestani, A.; Bajgholi, M.E. Influence of wc-based pin tool profile on microstructure and mechanical properties of AA1100 FSW welds. *Technologies* **2020**, *8*, 34. [CrossRef]

53. Kumar, K.; Kailas, S.V. The role of friction stir welding tool on material flow and weld formation. *Mater. Sci. Eng. A* **2008**, *485*, 367–374. [CrossRef]